ELSEVIER

Contents lists available at ScienceDirect

Journal of Alloys and Compounds

journal homepage: www.elsevier.com/locate/jalcom



Zero-dimensional antimony-based halides with efficient photoluminescence properties for visible light communication and nonlinear optics response

Yue Han ^a, Sijun Cao ^a, Peng He ^{a,*}, Peng Feng ^a, Hao Cui ^a, Xiaoliang Xu ^a, Xirong Ke ^a, Mengyue Wu ^b, Chen Chen ^{c,*}, Xiaosheng Tang ^{b,*}

ARTICLE INFO

Keywords: Organic-inorganic Metal halide Antimony-based Visible light communication Nonlinear optics effect

ABSTRACT

Zero-dimensional (OD) hybrid antimony-based halides have attracted significant attention owing to their mild synthesis conditions, remarkable light-emitting efficiency, and low toxicity. Nevertheless, it remains a challenge to develop OD antimony-based halides that simultaneously possess excellent optical properties and adaptability to diverse optoelectronic applications. In this study, we successfully synthesized two OD antimony-based halides, namely (C₄H₁₂N₂)₂SbCl₅(Cl)₂ (*R*-1) and (C₄H₁₂N₂)₄SbCl₆(Cl)₅·C₃H₇NO (*S*-1). Remarkably, *R*-1 exhibits excellent luminescence properties with a photoluminescence quantum yield (PLQY) of 92.29 %, significantly outperforming *S*-1 (57.08 %). Systematic investigations reveal their great potential for nonlinear optics, solid-state lighting, and visible light communication (VLC) applications. Specifically, the light-emitting diode (LED) based on *R*-1 achieves a superior color rendering index (CRI) of 90, outperforming the *S*-1-based device (CRI = 88). Furthermore, VLC with a high transmission data rate of 17.4 Mbps is achieved using the *S*-1-based LED. This study presents a highly efficient photoluminescent antimony-based halide system and validates its multifunctional applications across these advanced optoelectronic domains.

1. Introduction

In recent years, organic-inorganic metal halides (OIMHs) have emerged as a research hotspot in luminescent materials due to their outstanding optoelectronic properties [1–3], including tunable direct bandgap, high light absorption coefficients, and excellent charge transport capabilities [4,5]. By strategically modifying the types and structures of organic cations, researchers can construct materials with different dimensionalities (0D, 1D, 2D, and 3D) [6–9]. The structural diversity of 0D OIMHs enables flexible tunability of their luminescent properties [10–15]. Despite the remarkable progress of lead-based 0D OIMHs, environmental toxicity and stability issues severely limit their practical applications [16–19]. Consequently, the development of lead-free materials that combine high luminescence efficiency, superior stability, and better environmental compatibility than lead-based counterparts has become a critical research focus in this field.

In the development of lead-free OIMHs, researchers often prioritize

antimony-based systems because of their relatively good environmental compatibility (compared to lead-based alternatives) and unique 5 s² electronic configurations. These antimony-based halides exhibit remarkable potential for solid-state lighting the light-emitting diode (LED) applications owing to their distinctive broadband emission characteristics and tunable photophysical properties. Moreover, their superior white light emission performance enables their promising application in visible light communication (VLC) systems. Zhang et al. developed an Sb³⁺-doped 0D tin(IV)-based hybrid halide (C₁₀H₁₆N₂) SnCl₆:Sb, with a photoluminescence quantum yield (PLOY) of 77 % and successfully applied it in white LED devices with a superior color rendering index (CRI) of 84 [20]. Zhang et al. also reported two novel 0D antimony-based halides, (MTP)₆SbBr₆Sb₂Br₉·H₂O and (MTP)₂SbBr₅ for anti-counterfeiting technology [21]. Their synthesis required precise control of temperature and chemical stimuli, and both exhibited relatively low PLQYs (23.5 % for (MTP)₆SbBr₆Sb₂Br₉·H₂O and 57 % for (MTP)₂SbBr₅). Chen et al. synthesized (TEBA)₂SbCl_{5-x}Br_x (x = 0-5),

E-mail addresses: penghe@cqu.edu.cn (P. He), c.chen@cqu.edu.cn (C. Chen), xstang@cqu.edu.cn (X. Tang).

^a The Key Lab of Optoelectronic Technology and Systems, Ministry of Education, Chongqing University, Chongqing 400044, China

b School of Integrated Circuits, Chongqing University of Posts and Telecommunications, Chongqing 400065, China

^c School of Microelectronics and Communication Engineering, Chongaing University, Chongaing 400044, China

^{*} Corresponding authors.

tuning its photophysical properties and scintillation performance through halogen (Cl/Br) ratio adjustment [22]. Among these, (TEBA)_2SbCl_3Br_2 demonstrated optimal performance with a PLQY of 73.83 %. Toumi et al. reported a novel 0D hybrid antimony-based halide [(R)-C_8H_12N]_4(Sb_2Cl_{10}) [23]. While the study identified green emission from the material as potentially suitable for LED applications, the absence of specific device performance data limits conclusive evaluation of its practical viability. The single-component LED based on [C_{16}H_{33}(CH_3)_3N]_2SbCl_5 exhibits a PLQY of up to 1, but the CRI is only 70 [24]. To date, 0D organic-inorganic antimony-based halides with both high luminescence performance and applicability to multiple optoelectronic scenarios have rarely been reported.

In this study, we successfully synthesized two novel 0D organicinorganic hybrid antimony-based halides using (R)/(S)-3-aminopyrrolidine dihydrochloride and SbCl₃ as precursors. Systematic optical characterization reveals that under 360 nm UV excitation, R-1 exhibits a prominent orange broadband emission at 648 nm with an exceptional PLQY of 92.29 %, representing a 35 % enhancement compared to S-1 (57.08 %). Both crystals show large Stokes shifts (R-1:288 nm; S-1:270 nm), effectively reducing self-absorption and improving luminescent device performance. The second harmonic generation (SHG) characterization demonstrates the nonlinear optical applicability of R-1 and S-1. We fabricated LED devices incorporating R-1 and S-1 to evaluate their potential in solid-state lighting applications. The results demonstrate the significant promise of *R*-1 and *S*-1 for LED applications. Further investigations were conducted to evaluate the performances of R-1 and S-1 in VLC applications. This study provides valuable insights and methodologies for the design and synthesis of OIMHs and establishes an important foundation for their optoelectronic applications.

2. Result and discussion

2.1. Crystal structure

Here, two single crystals were synthesized at room temperature (RT) using the antisolvent diffusion method. This approach effectively addresses the challenges of conventional halides synthesis, including harsh high-temperature processes, high energy consumption, and difficult cost control, through mild reaction conditions. The synthesis involved dissolving organic molecules and SbCl3 in a 1:1 ratio in N, N-dimethylformamide. Crystallization was then induced by adding diethyl ether as the antisolvent, successfully yielding R-1 and S-1 single crystals (see Supporting Information for details). As illustrated in Fig. 1(a), the single-crystal X-ray diffraction (SCXRD) analysis of R-1 reveals that each antimony atom coordinates with six chlorine atoms, forming an [SbCl₆]³⁻ octahedral structure. These [SbCl₆]³⁻ units share Cl atoms, enabling closer packing and enhancing the rigidity and stability of the anionic octahedral framework. In addition, free chloride ions exist, while organic cations (C₄H₁₂N₂)²⁺ are interspersed within the octahedral voids, forming a typical OD crystal structure. The results show that R-1 crystallizes in the P2₁ 2₁ 2₁ space group with a unit cell configuration of a = 9.8239(6) Å, b = 9.9289(6) Å, c = 20.5107(12) Å, α $=\beta=\gamma=90^{\circ}$, and Z=4. The detailed crystal structure parameters are listed in Table S1. According to the SCXRD results, S-1 also crystallizes in the P2₁ 2₁ 2₁ space group, forming a 0D structure composed of (C₄H₁₂N₂)²⁺ cations, [SbCl₆]³⁻ anions, free chloride ions, and N, Ndimethylformamide molecules (Fig. 1(b)). The cations of R-1 and S-1 are shown in Fig. 1(c) and Fig. 1(d). Although S-1 shares the same space group with R-1, it exhibits different unit cell parameters. For S-1, the parameters are a = 9.5407(11) Å, b = 19.352(2) Å, c = 21.448(3) Å, α $=\beta=\gamma=90^{\circ},$ Z = 4 and more information is listed in Table S2.

To further investigate the crystal structures, we examined the morphologies of both crystals using the scanning electron microscopy

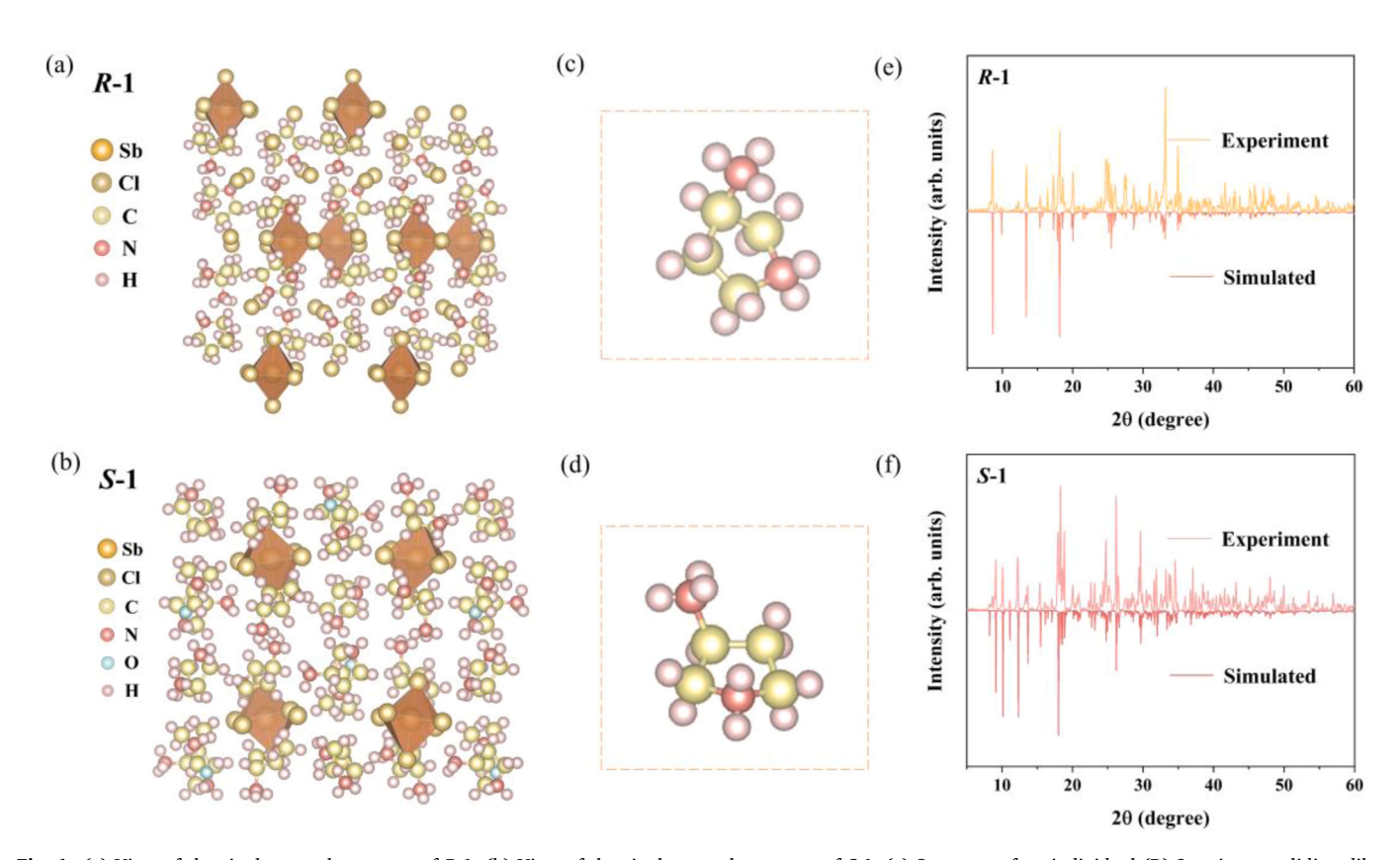


Fig. 1. (a) View of the single crystal structure of *R*-1. (b) View of the single crystal structure of *S*-1. (c) Structure of an individual (R)-3-aminopyrrolidine dihydrochloride. (d) Structure of an individual (S)-3-aminopyrrolidine dihydrochloride. (e) The PXRD patterns of *R*-1. (f) The PXRD patterns of *S*-1.

(SEM). The well-defined crystal shapes in Fig. S2 and Fig. S3 confirm their high crystallinity. Fig. S4 shows the energy-dispersive spectroscopy (EDS) mapping results, confirming the homogeneous distribution of C, N, Cl, and Sb atoms throughout the hybrid halide crystals. TGA was performed to investigate the thermal stability of the crystals. As shown in Fig. S5, R-1 and S-1 exhibited similar thermal stability characteristics. The materials exhibit negligible mass loss below approximately 250 °C and decomposition-initiated weight loss above this temperature threshold, demonstrating exceptional thermal stability. Furthermore, we ground the crystals into powder and verified the phase purity using powder X-ray diffraction (PXRD). Fig. 1(e) and Fig. 1(f) show that the experimental X-ray diffraction (XRD) patterns are in excellent agreement with the simulated patterns derived from single-crystal data, indicating the outstanding phase purity of the synthesized samples. Fig. 2(a) shows the X-ray photoelectron spectroscopy (XPS) results. which reflect the elemental composition of the samples. As Fig. S6 and Fig. S7 show, the Sb $3d_{5/2}$ peak appears at 530.1 eV, which indicates the presence of Sb³⁺, and the Cl 2p_{3/2} peak at 197.6 eV is consistent with typical Sb-Cl bonding characteristics. The C 1 s and N 1 s peaks correspond to the C-H and C-N bonds in the organic components, respectively.

2.2. Optical properties

Under 365 nm UV excitation, crystals *R*-1 and *S*-1 exhibited bright orange emissions (Fig. S1). The absorption spectra of the two crystals are shown in the lower panel of Fig. 2(b). In the 250–750 nm wavelength range, *R*-1 and *S*-1 displayed similar absorption features. Both crystals exhibit strong absorption peaks around 250 nm, and a moderate absorption band centered at 350–450 nm corresponds to ligand-to-metal charge transfer in the Sb-Cl octahedra. *R*-1 demonstrates a distinct absorption band in the 450–500 nm (blue-green region), indicating preferential absorption of blue-green light with complementary orange emission. *S*-1 absorption band appears broader, extending into the 500–550 nm, resulting in slightly longer-wavelength orange emission. Above 600 nm, *R*-1 and *S*-1 exhibit significantly attenuated absorption,

consistent with the optical behavior of orange-emitting materials that minimally absorb light in the red spectral region.

To systematically characterize the luminescence behavior, we measured the excitation and emission spectra of R-1 and S-1 (Fig. 2(c) and Fig. 2(d)). Owing to their similar compositions and structural features, we observe nearly identical steady-state photoluminescence excitation (PLE) and PL spectra. Under excitation at 360 nm and 362 nm respectively, R-1 and S-1 exhibit broad orange emission peaks with full width at half maximum (FWHM) of 126 nm and 174 nm, suggesting the self-trapped exciton (STE) emission mechanism [25]. The large Stokes shifts (R-1:288 nm; S-1:270 nm) further support STE-dominated luminescence [26]. In Sb^{3+} (5 s^2 electronic configuration) compounds, photoexcitation generates electron-hole pairs that form STEs through lattice distortion, leading to broad emission and large Stokes shifts [27]. This mechanism minimizes self-absorption and contributes to high-efficiency luminescence. Furthermore, because of the broad emission profiles of R-1 and S-1, we conducted excitation wavelength-dependent photoluminescence measurements (Fig. S8 and Fig. S9). The emission spectra exhibit negligible spectral shifts under different excitation wavelengths, confirming a single dominant emission center without interference from multiphase impurities.

To explore the factors affecting fluorescence intensity, we examined the decay behavior. Fig. 2(e) and Fig. 2(f) show the fluorescence decay curves measured at the optimal excitation wavelength. Curves are fitted by single exponential functions, yielding $\tau_{R-1}=3.94~\mu s$ and $\tau_{S-1}=3.82~\mu s$. The microsecond-scale lifetime components match the slow radiative recombination characteristic of STEs [28]. Using an integrating sphere fluorescence measurement system, we obtained PLQY of 92.29 % for R-1 and 57.08 % for S-1 (Fig. S10). Additionally, we conducted a systematic comparison of the PLQY values reported for antimony-based halides in the literature over the past three years (Table 1). Through comprehensive analysis, R-1 exhibits substantially enhanced PLQY performance, surpassing that of most previously reported counterparts.

Fig. 2(c) shows the circular dichroism (CD) and absorption spectra of R/S-1. For S-1, a prominent negative Cotton effect is observed around

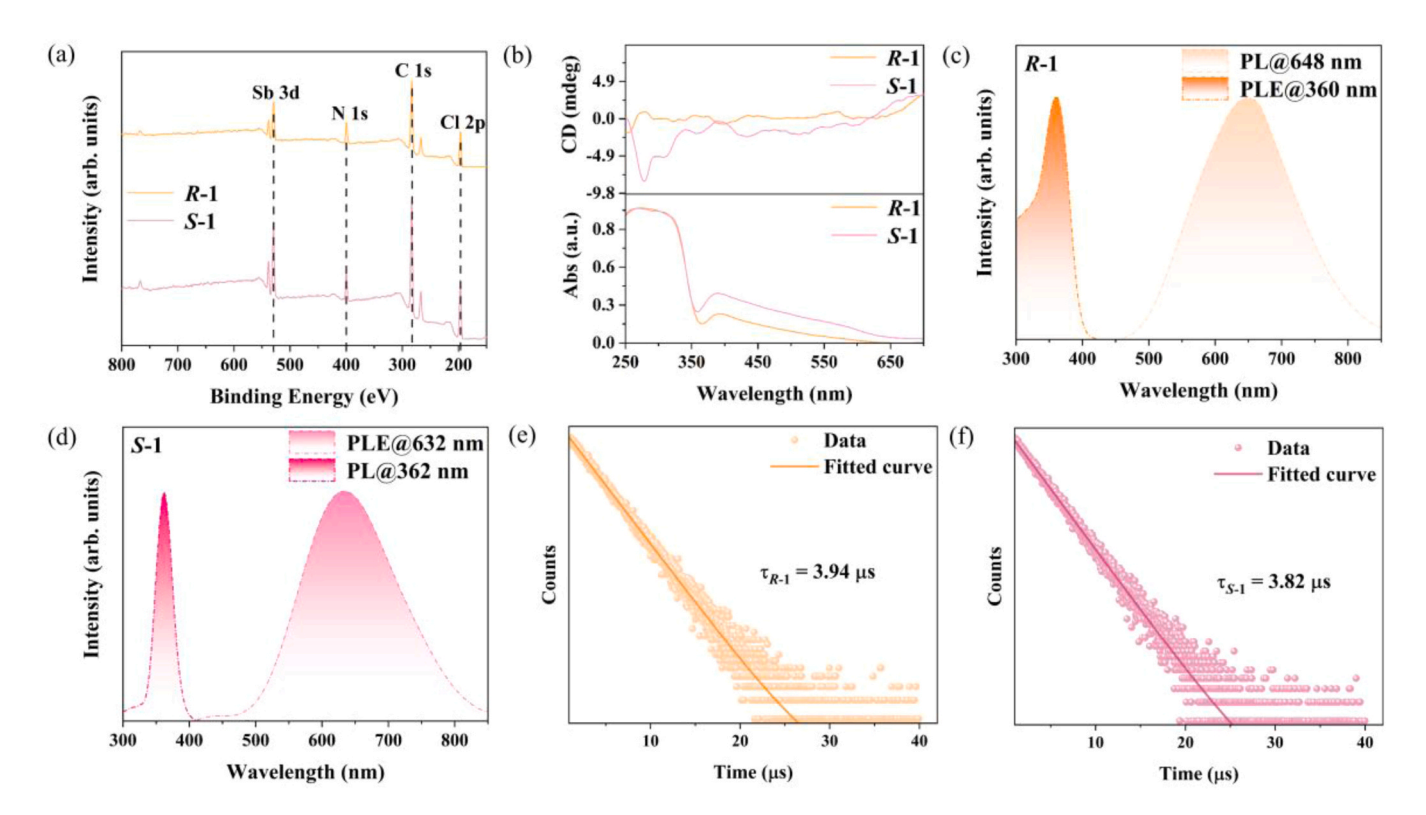


Fig. 2. (a) The X-ray photoelectron spectroscopy diagram of *R/S*-1. (b) The CD and absorption spectra of *R/S*-1. (c) PLE and PL spectra of *R*-1 single crystals at RT. (d) PLE and PL spectra of *S*-1 single crystals at RT. (e) Time-resolved PL decay dynamic of *R*-1. (f) Time-resolved PL decay dynamic of *S*-1.

Table 1PLQY Comparison of Antimony-Based Metal Halides.

Sample	PLQY	Reference
(TMS) ₂ SbCl ₅	90 %	[29]
[H ₂ BPZ][SbCl ₅]·H ₂ O	14.33 %	[30]
PEI(SbCl ₆) _n	28.80 %	[31]
$(C_{22}H_{24}P)_2SbCl_5$	83.50 %	[32]
(DFPD) ₆ SbCl ₉ ·2DMAC	90 %	[33]
[18 C@MA] ₂ SbCl ₅	88.58 %	[34]
S-1	57.08 %	This work
R-1	92.29 %	This work

250-300 nm, while R-1 shows relatively flat CD signals across the measured wavelength range. The CD signals show certain correspondence with both the absorption spectral features and peak positions.

To explore the influence of temperature on the luminescence properties of the crystals, we measured the PL spectra of R-1 and S-1 in the temperature range of 80-320 K (Fig. 3(a) and Fig. 3(d)), with the pseudo color map spectra in Fig. S11. As the temperature increases, the PL spectra of R-1 and S-1 show obvious shifts in peak positions and changes in intensity, reflecting the temperature dependence of the luminescence mechanisms. However, there are some differences in specific response characteristics. For R-1, within the low-temperature regime (80-200 K), as the temperature increases, the luminescence intensity continuously increases, and the peak position remains stable (the central wavelength around 625 nm). This indicates that the improvement in radiation recombination efficiency at low temperatures might result from the weakening of the carrier localization effects. In the range of 230-320 K, the PL intensity decreases significantly with increasing temperature. This conforms to the typical thermal quenching behavior, suggesting that non-radiative recombination channels are activated. Additionally, the PL peak gradually redshifts with increasing temperature, which mainly results from the enhancement of electron-phonon interaction and band gap reduction caused by lattice thermal expansion [35]. Similar to R-1, S-1 shows continuously increasing PL intensity in the 80-140 K range with no distinct peak shift (centered around

 $636\ nm).$ However, its PL intensity decreases with a clear redshift in the $170\text{--}320\ K$ range.

The exciton binding energy (E_b) can be calculated by fitting the emission peak intensity versus T^{-1} . E_b plays a decisive role in the radiative recombination mechanism, and is calculated as follows:

$$I_T = \frac{I_0}{1 + Ae^{\frac{-E_b}{TR_B}}} \tag{1}$$

where I_0 represents the integrated PL intensity at 0 K, A is the proportionality coefficient, and k_B denotes the Boltzmann constant [36]. The fitting results show that E_b for R-1 and S-1 are 379.51 meV and 595.75 meV, respectively (Fig. 3(b) and Fig. 3(e)). The high E_b creates a greater energy barrier, which effectively suppresses defect-assisted non-radiative transitions and enhances radiative recombination. Furthermore, by fitting the temperature-dependent FWHM data, the Huang-Rhys factor (S), which reflects the exciton-phonon coupling strength, can be determined using the following equation:

$$FWHM = 2.36\sqrt{S}\hbar\omega_{phonon}\sqrt{\coth\left(\frac{\hbar\omega_{phonon}}{2k_{B}T}\right)}$$
 (2)

where *FWHM* refers to the width of the emission peak at half of its maximum intensity under different temperature conditions; $\hbar\omega$ represents the energy associated with lattice vibrations; and k_B denotes the Boltzmann constant [36]. As shown in Fig. 3(c) and Fig. 3(f), the fitting results reveal that R-1 exhibits a phonon energy of 33.56 meV with a Huang-Rhys factor of 19.96, while S-1 demonstrates a higher phonon energy of 40.23 meV and a lower Huang-Rhys factor of 15.91. These parameters demonstrate that S-1 exhibits higher phonon energy and lower Huang-Rhys factor compared to R-1, indicating relatively weaker electron-phonon coupling in S-1, which likely favors radiative recombination of charge carriers. Moreover, the elevated phonon energy implies stronger exciton confinement by lattice vibrations, which facilitates the formation of stable STEs and consequently leads to highly efficient broadband emissions. Furthermore, the reduced Huang-Rhys

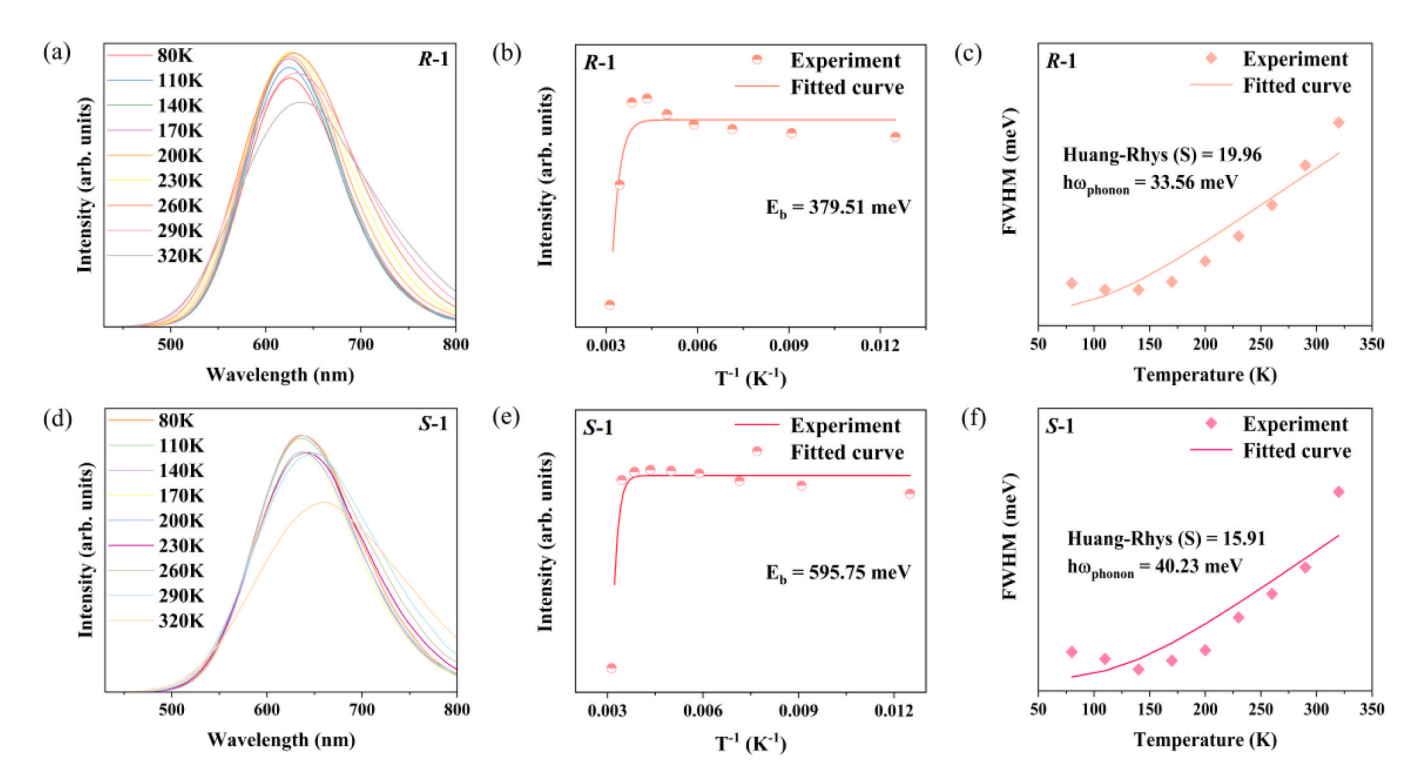


Fig. 3. (a) Temperature-dependent PL spectra of *R*-1. (b) Nonlinear fitted PL intensity-1/T spectrum of *R*-1. (c) Fitted *FWHM*-temperature spectrum of *R*-1. (d) Temperature-dependent PL spectra of *S*-1. (e) Nonlinear fitted PL intensity-1/T spectrum of *S*-1. (f) Fitted *FWHM*-temperature spectrum of *S*-1.

factor implies a relatively minor contribution from non-radiative recombination channels. In summary, these characteristic parameters confirm the existence of STEs in both materials, with *S*-1 displaying superior exciton confinement and more pronounced radiative recombination advantages. In most antimony-based halides reported in relevant literature, STE emission is achieved through strong lattice distortion, which however often leads to excessive non-radiative recombination. For example, (TEBA)₂SbCl₃Br₂ [22] relies on severe distortion of [SbCl₃Br₂]³⁻ octahedra to form STEs. This process results in a relatively high Huang-Rhys factor (S \approx 22) and a rather low PLQY of only 73.83 %. In contrast, *R*-1 and *S*-1 adopt a "moderate-weak" lattice distortion strategy, effectively avoiding the aforementioned drawbacks. Without DMF molecules, *R*-1 exhibits dense packing of [SbCl₆] $^{3-}$

octahedra (unit cell parameters: a = 9.8239 Å, b = 9.9289 Å), leading to moderate lattice distortion (Huang-Rhys factor S = 19.96). This degree of distortion skillfully balances the STE formation efficiency and radiative recombination rate, ultimately achieving a high PLQY of 92.29 %. For S-1, the introduction of DMF molecules loosens the packing of $[SbCl_6]$ ³⁻ octahedra (unit cell parameters: a=9.5407 Å, b=19.352 Å), resulting in weak lattice distortion (Huang-Rhys factor S = 15.91), and this weak distortion can enhance exciton localization. Furthermore, typical antimony-based halides in the literature [(R)-C₈H₁₂N]₄(Sb₂Cl₁₀)) exhibit weak electron-phonon coupling (phonon energy \approx 25 meV), which leads to poor exciton confinement capability [23]. In contrast, both R-1 and S-1 show stronger electron-phonon coupling, with phonon energies of 33.56 meV and

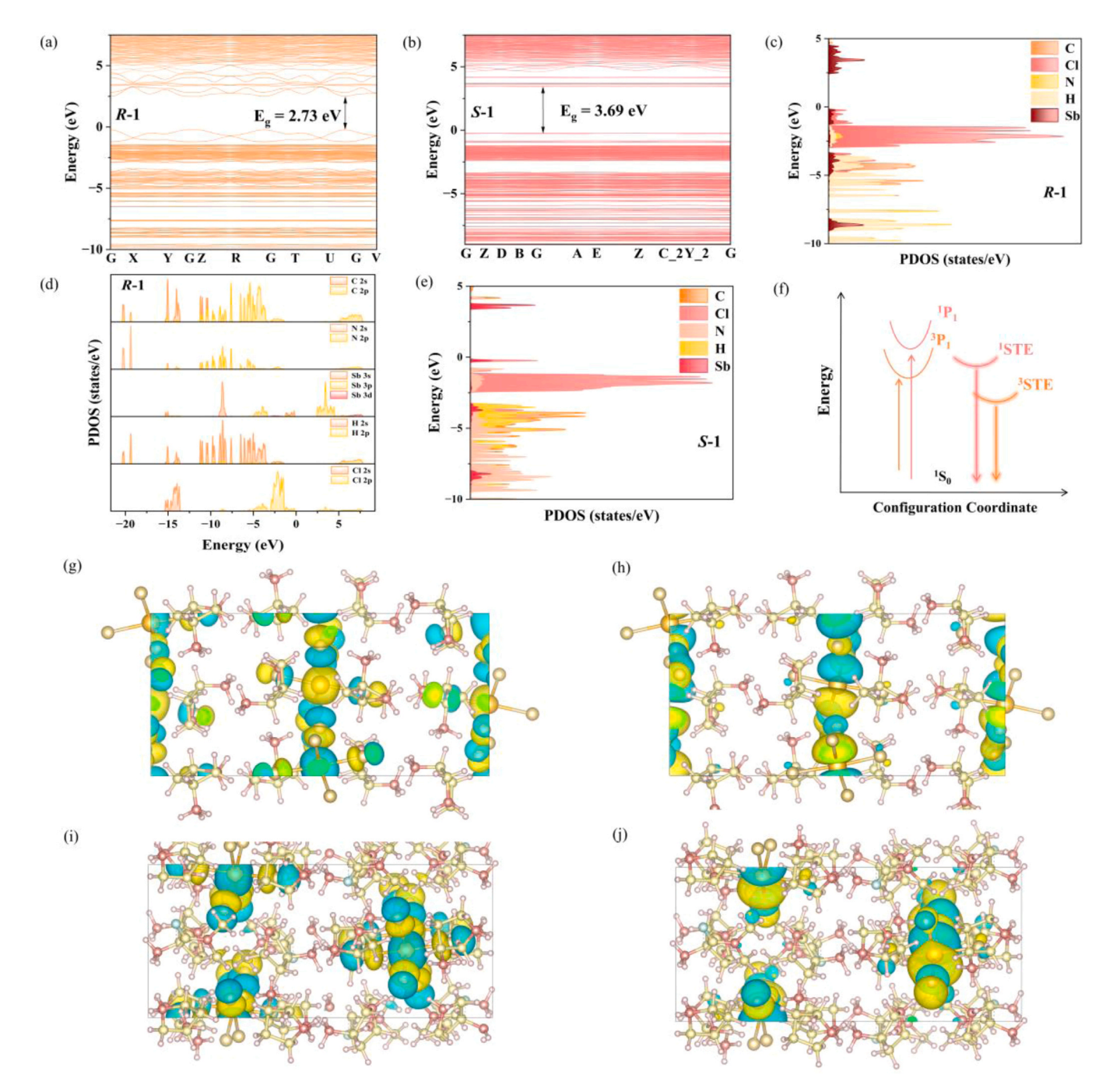


Fig. 4. (a) Simulated band structure of *R*-1. (b) Simulated band structure of *S*-1. (c) Projected density of states of *R*-1. (d) Projected density of states of different atomic orbitals of *R*-1. (e) Projected density of states of *S*-1. (f) Electronic charge distribution of *R*-1 and *S*-1. (g) The LUMO in *R*-1. (h) The HOMO in *R*-1. (i) The LUMO in *S*-1.

40.23 meV, respectively. The high phonon energy can promote the rapid relaxation of triplet excited states to triplet STEs and effectively suppress exciton dissociation, ensuring stable STE emission of the materials even at room temperature.

To deeply understand the excited-state dynamics behavior of $\it R-1$ and $\it S-1$, we measured the fluorescence decay curves from 80 K to 290 K (Fig. S12). The results show the fluorescence lifetimes of $\it R-1$ and $\it S-1$ exhibit significant temperature dependence. In the range of 80 K to 290 K, the fluorescence decay curve exhibits a single exponential decay characteristic, with the fitted lifetimes being $\tau_{\it R-1}=3.9~\mu s$ and $\tau_{\it S-1}=3.8~\mu s$ us.

First-principles calculations based on density functional theory (DFT) were performed to gain deeper insights into the luminescence mechanisms of R-1 and S-1. Perdew-Burke-Ernzerhof (PBE) generalized gradient approximation (GGA) functional was employed to treat electron exchange-correlation interactions. The calculation results reveal the direct bandgap values of R-1 and S-1 are 2.73 eV and 3.69 eV, respectively (Fig. 4(a) and Fig. 4(b)). Compared with experimental measurements, the PBE functional calculations exhibit characteristic band gap underestimation, which is consistent with the known limitations of this functional in band gap predictions [37] (Fig. S13). According to the projected density of states (PDOS) analysis of R-1 (Fig. 4 (c)), the valence band maximum (VBM) is primarily attributed to antimony and chlorine atoms, while the conduction band minimum (CBM) is mainly determined by antimony atoms. Specifically, the 3p orbitals of antimony and 2p orbitals of chlorine play dominant roles in these contributions (Fig. 4(d)). Similarly, Fig. 4(e) shows that both the VBM and CBM of S-1 are predominantly formed by antimony and chlorine atoms, with the contributing orbitals being identical to those in R-1. The electron localization density distribution further confirms these conclusions, clearly revealing the spatial distribution characteristics of the highest occupied molecular orbital (HOMO) and lowest unoccupied molecular orbital (LUMO) in both R-1 and S-1 (Fig. 4g-j).

Based on the experimental results, we conclude that the broad orange emission observed in both R-1 and S-1 originates from the STEs localized on the Sb³⁺ ions. As illustrated in Fig. 4(f), the photophysical

process involves an initial electronic transition from the ground state (1S_0) to the singlet excited state (1P_1) of Sb^{3+} under photoexcitation. Owing to the strong spin-orbit coupling in heavy Sb^{3+} ions, the initially populated 1P_1 state rapidly undergoes intersystem crossing to the triplet excited state (3P_1), which subsequently relaxes into a triplet STE through strong electron-phonon coupling. The inherent lattice distortions in R-1 and S-1 facilitate this self-trapping process by lowering the energy barrier between free exciton and STE states, enabling efficient STE formation and emission even at RT. The characteristic broad emission spectra arise from the strong coupling between STE states and lattice vibrational modes, while the microsecond-scale luminescence lifetimes (3.94 μ s for R-1 and 3.82 μ s for S-1) are consistent with the radiative decay of triplet STEs. In general, these findings demonstrate that the luminescence in R-1 and S-1 is primarily governed by the radiative recombination of Sb^{3+} -centered STEs.

2.3. The second harmonic generation

The SHG is an important indicator for evaluating the nonlinear optical properties of crystals, and it can effectively reflect the frequency conversion capability of the material under the action of a strong light field. As shown in Fig. 5(a), under the excitation of 1064 nm fundamental light, *R*-1 exhibits a strong second-harmonic signal response, and its intensity is clearly superior to that of *S*-1. Both crystals show the peaks in the range of 450–650 nm (corresponding to the 532 nm second harmonic wavelength), but the *FWHM* of *R*-1 is narrower, indicating a more uniform microstructure and fewer defect scattering centers. Under the excitation of 1540 nm fundamental light (corresponding to the 770 nm second harmonic wavelength), *R*-1 also shows excellent nonlinear optical performance. In the wavelength range of 650–850 nm, the second harmonic signal intensity of *R*-1 is significantly higher than that of *S*-1, which is consistent with the results under 1064 nm excitation.

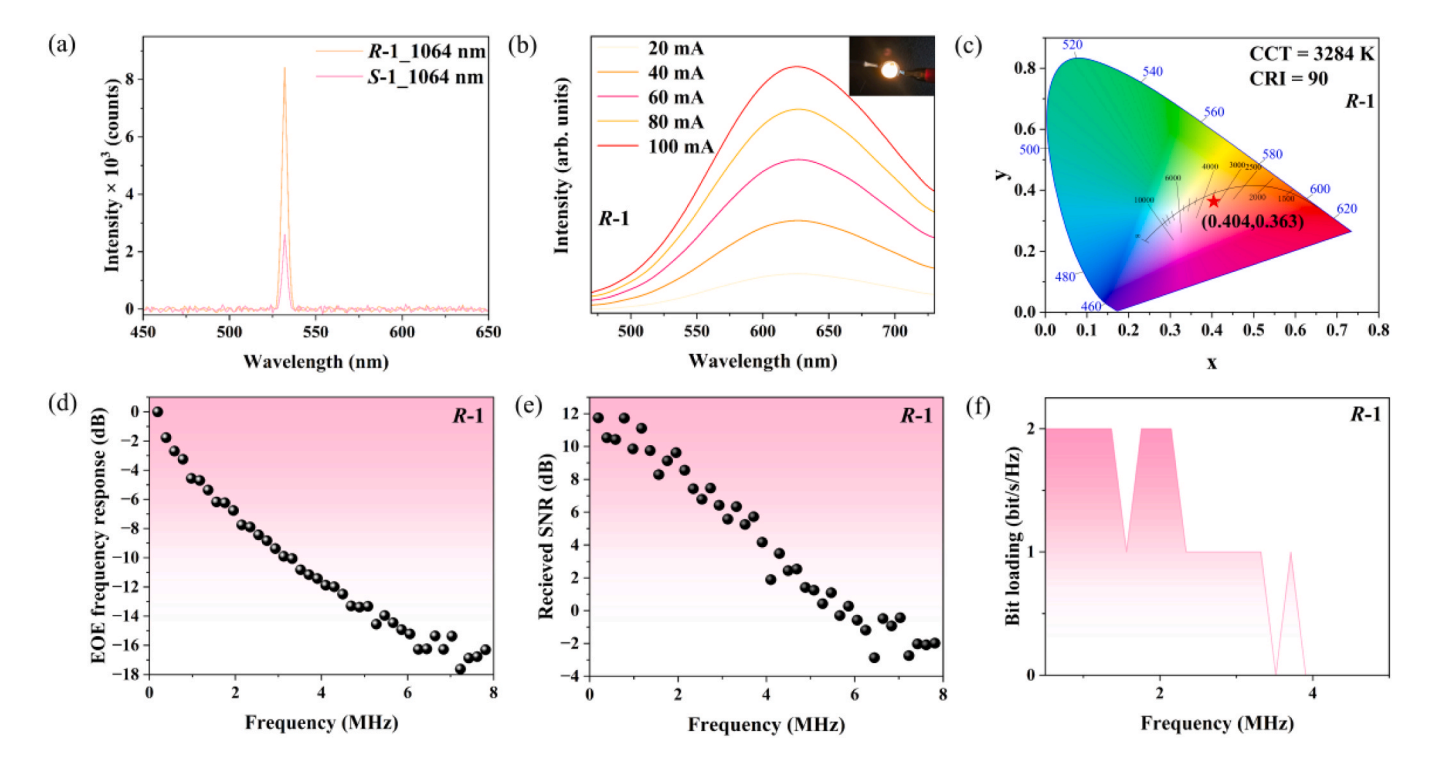


Fig. 5. (a) The SHG signals of *R/S*-1 under 1064 nm excitations. (b) The emission spectra of *S*-1-based LED under different driving currents. (c) CIE chromaticity coordinate of *S*-1-LED. (d) The EOE frequency response. (e) Frequency-dependent received SNR. (f) The bit loading profile of the VLC system based on *R*-1-LED.

2.4. Visible light communication

Metal halides have shown promising application prospects in the fields of solid-state lighting and VLC due to their excellent photoelectric properties. Here, we fabricated high-performance LED devices using 0D antimony-based samples R-1 and S-1. Specifically, we ground R-1 and S-1 into fine powders, evenly coated them on the surface of a 365 nm ultraviolet LED chip, and encapsulated them with transparent silicone to form LED devices. The LED device based on R-1 emits warm white light, with a correlated color temperature (CCT) of 3284 K, a color coordinate (CIE 1931) of (0.404, 0.363), and a color rendering index (CRI) of 90 (Fig. 5(c)), while the LED prepared with S-1 shows cold white light emission with a CCT of 5007 K, a color coordinate (CIE 1931) of (0.345, 0.372), and a CRI of 88 (Fig. S14). In addition, the comparison of CRI among single-component LED devices demonstrates that our fabricated LED devices achieve superior CRI performance (Table 2). Both devices exhibit excellent stability under different forward bias currents (20-100 mA), with their luminous intensity increasing linearly with the driving current (Fig. 5(b) and Fig. S14(a)). In addition, we tested the performance of the fabricated LEDs after 12 hours of continuous operation. The results are shown in Fig. S15, indicating that the performance of both LEDs hardly changed. These outstanding performance parameters fully demonstrate the practical application value of R-1 and S-1 in eco-friendly solid-state lighting devices, providing new material options for the development of high-performance white LED technologies.

To further exploit their performance in VLC systems, we utilized the LEDs mentioned above as information carriers for optical signal transmissions. The LED fabricated with S-1 exhibits superior performance, with an electro-optic-electrical (EOE) frequency response bandwidth of 2 MHz (-3 dB) (Fig. S16(a)), which is significantly higher than the 1 MHz bandwidth of the R-1 LED (Fig. 5(d)). In addition, the S-1-LEDbased VLC system achieves outstanding performance with a superior signal-to-noise ratio (SNR) exceeding 15 dB above the -3 dB cutoff frequency. In comparison, the VLC system based on R-1-LED demonstrates a lower SNR of approximately 10 dB under identical conditions (Fig. 5(e) and Fig. S16(b)). Furthermore, we implemented an orthogonal frequency division multiplexing (OFDM) modulation scheme with adaptive bit-loading capability to thoroughly investigate the achievable transmission data rates. Fig. 5(f) and Fig. S16(c) show the bit loading profiles of VLC system based on S-1-LED and R-1-LED, respectively. We observe that the S-1 LED achieves a higher bit-loading efficiency of 4 bit/s/Hz in the low-frequency region, compared to only 2 bit/s/Hz for the R-1 LED, which is closely related to their bandwidth properties. Moreover, the corresponding received constellation diagrams of binary phase-shift keying (BPSK), 4-ary quadrature amplitude modulation (4QAM) and 8QAM are shown in Fig. S17 and Fig. S18, which provide important guidance for the adaptive modulation strategy selection in practical VLC applications. The S-1-LED-based VLC system employing adaptive bit-loading OFDM modulation achieves a transmission data rate of 17.4 Mbps, demonstrating significant improvement over the 5.5 Mbps data rate attained by the R-1-LED system. These results highlight the great potential of R-1 and S-1 for high-performance white LEDs and efficient VLC systems.

3. Conclusion

In conclusion, we have synthesized two novel 0D antimony-based single crystals (R-1 and S-1) using a RT antisolvent diffusion method, which demonstrate exceptional promise for optoelectronic applications. Detailed structural and optical analyses reveal that both materials exhibit efficient broadband orange emission originating from STEs, with outstanding PLQY of up to 92.29 %. The crystals show remarkable nonlinear optical properties, particularly in SHG, along with excellent performance in white LED devices and VLC systems. Both LEDs exhibit relatively high CRI (90 and 88). Moreover, the fabricated LEDs are utilized for VLC, where the S-1-based LED have achieved a -3 dB

Table 2 CRI and -3 dB Bandwidth Comparison.

Sample	CRI	-3dB bandwidth	Reference
MA ₂ CuCl ₃	63.27		[38]
[C ₁₆ H ₃₃ (CH ₃) ₃ N] ₂ SbCl ₅	70		[24]
BA ₆ InCl ₉ : Sb	86.14		[39]
InCl ₃ -TPOBD	84.8		[40]
DPCu ₄ I ₆	85.1		[41]
Cs ₃ Cu ₂ Cl ₅	94	0.42 MHz	[42]
DDAB-CsPbBr ₃	88	1.5 MHz	[43]
S-1	88	2 MHz	This work
R-1	90	1 MHz	This work

bandwidth of 2 MHz and transmission data rate of 17.4 Mbps with OFDM modulation. These antimony-based materials have achieved a balance of solution-processable synthesis and superior optoelectronic performance. They are alternatives for next-generation solid-state lighting and VLC applications, addressing the critical need for substitutes to lead-based materials with antimony compounds demonstrating greater environmental compatibility than lead-based counterparts. This work not only synthesized novel 0D antimony-based halides with high luminescence performance but also provided practical guidelines for their implementation in optoelectronic devices.

CRediT authorship contribution statement

Chen Chen: Writing – review & editing, Supervision, Conceptualization. Xiaosheng Tang: Writing – review & editing, Supervision, Conceptualization. Xirong Ke: Methodology, Investigation. Mengyue Wu: Methodology, Investigation. Yue Han: Writing – original draft, Methodology, Investigation, Formal analysis. Sijun Cao: Visualization, Methodology, Investigation. Hao Cui: Methodology, Investigation. Xiaoliang Xu: Methodology, Investigation. Peng He: Writing – review & editing, Supervision, Methodology. Peng Feng: Methodology, Investigation.

Declaration of Competing Interest

The authors declare that they have no known competing financial interests or personal relationships that could have appeared to influence the work reported in this paper.

Acknowledgements

This work was supported by the National Natural Science Foundation of China (No. 62375032, 62104023, 52302059), Natural Science Foundation of Chongqing (No. CSTB2023TIAD-KPX0017, CSTB2022NSCQ-MSX0360), the Fundamental Research Funds for the Central Universities (No. 2024CDJYXTD-009, 2025CDJZKZCQ-01), The Open Fund of the State Key Laboratory of High Field Laser Physics (Shanghai Institute of Optics and Fine Mechanics). China Postdoctoral Science Foundation (No. BX20230355). Sponsored by Natural Science Foundation of Chongqing, China, cstc2019jcyj-msxmX0737. Supported by the Science and Technology Research Program of Chongqing Municipal Education Commission (No. KJQN202400619).

Appendix A. Supporting information

Supplementary data associated with this article can be found in the online version at doi:10.1016/j.jallcom.2025.184506.

References

- [1] Y. Dong, Y. Han, R. Chen, Y. Lin, B.-B. Cui, Recent progress of triplet state emission in organic-inorganic hybrid metal halides, J. Lumin. 249 (2022).
- [2] L. Kang, Z. Lin, Regulation strategy of White emission from organic-inorganic hybrid metal halide perovskites, Inorg. Chem. Front. 10 (2023) 13–36.

- [3] Q. Zhou, W. Li, J. Xiao, A. Li, X. Han, Low-Dimensional metal halide for high performance scintillators, Adv. Funct. Mater. 34 (2024).
- [4] T. Chang, Y. Dai, Q. Wei, X. Xu, S. Cao, B. Zou, Q. Zhang, R. Zeng, Temperature-Dependent reversible optical properties of Mn-Based Organic-Inorganic hybrid (C8H20N)2MnCl4 metal halides, ACS Appl. Mater. Interfaces 15 (2023) 5487–5494.
- [5] L. Liu, Y. Tang, Y. Ma, B. Hu, Spin-Orbital ordering effects of light emission in Organic-Inorganic hybrid metal halide perovskites, Adv. Mater. (2024) 2411913.
- [6] P. Acharyya, K. Kundu, K. Biswas, 2D layered all-inorganic halide perovskites: recent trends in their structure, synthesis and properties, Nanoscale 12 (2020) 21094–21117.
- [7] L. He, P. Cao, Z.-N. Zhou, Y.-W. Yang, L.-Q. Chen, Q. Ye, Alkali metal substitution for modulating Three-Dimensional halide double perovskite ferroelectric, Inorg. Chem. 64 (2025) 8455–8462.
- [8] A. Pradhan, S. Sahoo, S.L. Samal, C2H5NH3)2BiCl5—xBrx perovskites containing 1D chains: effect of br substitution on their structural and optical properties, CrystEngComm 26 (2024) 312–323.
- [9] Y. Zhang, G. Zhang, L. Zhu, Y. Li, T. Zhang, F. Hao, L. Meng, H. Xie, H. Liu, Z. Tang, Blue-excited broadband near-infrared emission from zero-dimensional organicinorganic hybrid metal halides, J. Colloid Interface Sci. 686 (2025) 37–44.
- [10] A. Fandouli, N.B. Hamadi, A. Guesmi, E.C. Sañudo, X. Zarate, M.-S. Torres, E. Schott, A. Houas, A. Rayes, Synthesis, structure, and luminescence properties of a OD organic-inorganic cadmium iodide: combined experimental and theoretical approach, J. Mol. Struct. (2024) 1314.
- [11] H. Ferjani, O.M. Lemine, Y. Ben Smida, N. Salah, H. Kaouach, F. Saadi, H.I. Wahbi, M.Y. Almashnowi, R. Ramadan, D.C. Onwudiwe, Visible emission from a zerodimensional tin-based organic-inorganic metal halide for luminescent devices: experimental and theoretical investigation, J. Mol. Struct. (2025) 1327.
- [12] D. Li, X. Sun, S. Jiao, W. Zhang, Y. Lu, M. Zhao, Y. Wu, H.-L. Cai, X. Wu, A novel zero-dimensional organic-inorganic hybrid ferroelectric material, J. Mater. Chem. C. 12 (2024) 4267–4272.
- [13] Y. Li, N. He, B. Xu, L. Dong, X. Zhang, J. Xu, P. Gong, Z. Lin, Synthesis, structure, and optical properties of a 0D hybrid Organic–Inorganic metal halide (C5N2H14Cl) GeCl3, Inorg. Chem. 63 (2024) 4412–4418.
- [14] C. Peng, J. Wei, L. Duan, Y. Tian, Q. Wei, Mn(II)-Activated Zero-Dimensional Zinc (II)-Based metal halide hybrids with Near-Unity photoluminescence quantum vield, Materials 17 (2024).
- [15] C. Zhou, H. Lin, Q. He, L. Xu, M. Worku, M. Chaaban, S. Lee, X. Shi, M.-H. Du, B. Ma, Low dimensional metal halide perovskites and hybrids, Materials Science Engineering R Reports 137 (2019) 38–65.
- [16] P. Priyadarshini, S. Senapati, R. Naik, Lead-free organic inorganic hybrid halide perovskites: an emerging candidate for bifunctional applications, Renew. Sustain. Energy Rev. (2023) 186.
- [17] G. Song, M. Li, Y. Yang, F. Liang, Q. Huang, X. Liu, P. Gong, Z. Xia, Z. Lin, Lead-Free Tin(IV)-Based Organic-Inorganic metal halide hybrids with excellent stability and Blue-Broadband emission. J. Phys. Chem. Lett. 11 (2020) 1808–1813.
- [18] Z. Tang, X. Wang, T. Bai, S. Liu, S. Wang, Q. Wei, B. Fan, J. Chen, High-Efficiency luminescence and robust thermal quenching resistance in Organic–Inorganic hybrid Indium-Based metal halides. Adv. Ont. Mater. 13 (2024).
- hybrid Indium-Based metal halides, Adv. Opt. Mater. 13 (2024).

 [19] H. Zhou, Z. Liu, X. Yun, H. Hu, H. Zhong, H. Li, Y. Shi, Efficient blue emission in Organic–Inorganic metal halide (TEA)2InCl5 triggered by Bi3+-Doping, Adv. Mater. Technol. 10 (2024).
- [20] G. Zhang, P. Dang, H. Xiao, H. Lian, S. Liang, L. Yang, Z. Cheng, G. Li, J. Lin, Antimony-Doped Lead-Free Zero-Dimensional Tin(IV)-Based Organic-Inorganic metal halide hybrids with high photoluminescence quantum yield and remarkable stability, Adv. Opt. Mater. 9 (2021).
- [21] B. Li, J. Jin, M. Yin, X. Zhang, M.S. Molokeev, Z. Xia, Y. Xu, Sequential and reversible phase transformations in Zero-Dimensional Organic-Inorganic hybrid Sb-based halides towards multiple emissions, Angew. Chem. Int. Ed. 61 (2022).
- [22] H. Chen, H. Cui, T. Jiang, Z. Feng, Y. Yan, S. Liu, Q. Zhao, Highly luminescent antimony-based organic-inorganic hybrid halides for X-ray imaging and detection, J. Mater. Chem. C. 12 (2024) 12325–12331.
- [23] E. Toumi, N. Elleuch, S. Shova, M. Boujelbene, Structural asymmetry, physicochemical characterization and optical properties of a new luminescent zero dimensional organic-inorganic hybrid compound, Results Chem. 12 (2024).

- [24] S. Sui, C. Wang, G. Hu, Y. Li, W. Meng, J. Luo, G. Xu, Z. Deng, Bright and stable quaternary ammonium antimony halides for solid-state lighting, J. Mater. Chem. C. 10 (2022) 8938–8946.
- [25] A. Biswas, R. Bakthavatsalam, B.P. Mali, V. Bahadur, C. Biswas, S.S.K. Raavi, R. G. Gonnade, J. Kundu, The metal halide structure and the extent of distortion control the photo-physical properties of luminescent zero dimensional organicantimony(iii) halide hybrids, J. Mater. Chem. C. 9 (2021) 348–358.
- [26] L. Li, Z. Chen, B. Gao, Q. Xu, CO2 Pressure-Induced Self-Trapped excitons in SrTiO3, Adv. Photonics Res. 5 (2024).
- [27] Z. Wang, X. Wang, Z. Chen, Y. Liu, H. Xie, J. Xue, L. Mao, Y. Yan, H. Lu, Turn-on circularly polarized luminescence in chiral indium chlorides by 5s2 metal centers, Angew. Chem. Int. Ed. 62 (2023).
- [28] J.-B. Luo, J.-H. Wei, Z.-Z. Zhang, D.-B. Kuang, Water-Molecule-Induced emission transformation of Zero-Dimension Antimony-Based metal halide, Inorg. Chem. 61 (2021) 338–345.
- [29] J.F. Liao, Z. Zhang, L. Zhou, Z. Tang, G. Xing, Achieving Near-Unity red light photoluminescence in antimony halide crystals via polyhedron regulation, Angew. Chem. Int. Ed. 63 (2024).
- [30] Y.-C. Peng, H.-W. Lin, S.-H. Zhou, J.-C. Jin, T.-H. Zhuang, A. Ablez, Z.-P. Wang, K.-Z. Du, X.-Y. Huang, Reversible luminescent switching induced by Heat/Water treatment in a Zero-Dimensional hybrid Antimony(III) chloride, Molecules 28 (2023).
- [31] S.S. Li, P. Cheng, H. Liu, J. Li, S. Wang, C. Xiao, J. Liu, J. Chen, K. Wu, Polymeric metal halides with bright luminescence and versatile processability, Angew. Chem. Int. Ed. 63 (2024).
- [32] Z. Zang, D. Liang, Y. Shi, Z. Liu, R. Li, S.M.H. Qaid, W. Cai, Ethanol-Induced reversible phase transition in antimony halides for morse code Anti-Counterfeiting and optical logic gates, Laser Photonics Rev. 19 (2024).
- [33] X. Wang, T. Bai, J. Sun, J. Liu, Y. Su, J. Chen, The effect of solvent on the formation of low-dimensional metal halides and their self-trapped exciton emission, Chem. Eng. J. 486 (2024).
- [34] Ch Wei, S. Dong, Z. Xu, M. Li, T. Zhang, Z. Xu, S. Lan, S. Wang, L. Mao, Controllable Multi-Exciton Zero-Dimensional Antimony-Based metal halides for White-light emission and β-Ray detection, Angew. Chem. Int. Ed. 63 (2024).
- [35] W. Ma, T. Jiang, Z. Yang, H. Zhang, Y. Su, Z. Chen, X. Chen, Y. Ma, W. Zhu, X. Yu, H. Zhu, J. Qiu, X. Liu, X. Xu, Y. Yang, Highly resolved and robust dynamic X-Ray imaging using perovskite Glass-Ceramic scintillator with reduced light scattering, Adv. Sci. 8 (2021).
- [36] D.-Y. Li, Y.-B. Shang, Q. Liu, H.-W. Zhang, X.-Y. Zhang, C.-Y. Yue, X.-W. Lei, 0D hybrid indium halide as a highly efficient X-ray scintillation and ultra-sensitive fluorescent probe, Mater. Horiz. 10 (2023) 5004–5015.
- [37] H. Peng, Y. Tian, X. Wang, T. Huang, Z. Yu, Y. Zhao, T. Dong, J. Wang, B. Zou, Pure White emission with 91.9% photoluminescence quantum yield of [(C3H7)4N] 2Cu2l4 out of polaronic states and Ultra-High color rendering index, ACS Appl. Mater. Interfaces 14 (2022) 12395–12403.
- [38] X. Meng, S. Ji, Q. Wang, X. Wang, T. Bai, R. Zhang, B. Yang, Y. Li, Z. Shao, J. Jiang, Kl Han, F. Liu, Organic-Inorganic hybrid Cuprous-Based metal halides for warm White Light-Emitting diodes. Adv. Sci. 9 (2022).
- [39] Z. Tang, X. Meng, H. Zhao, S. Ji, Q. Wang, T. Bai, R. Zhang, J. Jiang, C. Katan, J. Even, F. Liu, Moisture-Insensitive, Phase-Stable Indium-Based metal halides and their Light-Emitting applications, Adv. Opt. Mater. 12 (2023).
- [40] T. Chen, Y.J. Ma, D. Yan, Single-Component 0D Metal-Organic halides with Color-Variable Long-Afterglow toward Multi-Level information security and White-Light LED, Adv. Funct. Mater. 33 (2023).
- [41] S. Zhou, Y. Chen, K. Li, X. Liu, T. Zhang, W. Shen, M. Li, L. Zhou, R. He, Photophysical studies for Cu(I)-based halides: broad excitation bands and highly efficient single-component warm White-light-emitting diodes, Chem. Sci. 14 (2023) 5415-5424
- [42] S. Zhao, C. Chen, W. Cai, R. Li, H. Li, S. Jiang, M. Liu, Z. Zang, Efficiently luminescent and stable Lead-free Cs3Cu2Cl5@Silica nanocrystals for White Light-Emitting diodes and communication, Adv. Opt. Mater. 9 (2021).
- [43] X. Li, W. Cai, H. Guan, S. Zhao, S. Cao, C. Chen, M. Liu, Z. Zang, Highly stable CsPbBr3 quantum dots by silica-coating and ligand modification for White lightemitting diodes and visible light communication, Chem. Eng. J. 419 (2021).